Available online at www.sciencedirect.com
ScienceDirect
Dynamics of Atmospheres and Oceans 42 (2006) 107–126
dynamics of atmospheres and oceans
www.elsevier.com/locate/dynatmoce

Analysis of rainfall characteristics of the Madden–Julian oscillation using TRMM satellite data

Juntaro Morita [a,1], Yukari N. Takayabu [a,*], Shoichi Shige [b], Yasumasa Kodama [c]

[a] Center for Climate System Research, University of Tokyo, Tokyo, Japan
[b] Department of Aerospace Engineering, Osaka Prefecture University, Osaka, Japan
[c] Hirosaki University, Aomori, Japan

Available online 4 October 2006

Abstract

Rainfall characteristics of the Madden–Julian oscillation (MJO) are analyzed primarily using tropical rainfall measuring mission (TRMM) precipitation radar (PR), TRMM microwave imager (TMI) and lighting imaging sensor (LIS) data. Latent heating structure is also examined using latent heating data estimated with the spectral latent heating (SLH) algorithm.

The zonal structure, time evolution, and characteristic stages of the MJO precipitation system are described. Stratiform rain fraction increases with the cloud activity, and the amplitude of stratiform rain variation associated with the MJO is larger than that of convective rain by a factor of 1.7. Maximum peaks of both convective rain and stratiform rain precede the minimum peak of the outgoing longwave radiation (OLR) anomaly which is often used as a proxy for the MJO convection. Stratiform rain remains longer than convective rain until ∼4000 km behind the peak of the mature phase. The stratiform rain contribution results in the top-heavy heating profile of the MJO.

Associated with the MJO, there are tri-pole convective rain top heights (RTH) at 10–11, ∼7 and ∼3 km, corresponding to the dominance of afternoon showers, organized systems, and shallow convections, respectively. The stratiform rain is basically organized with convective rain, having similar but slightly lower RTH and slightly lags the convective rain maximum. It is notable that relatively moderate (∼7 km) RTH is dominant in the mature phase of the MJO, while very tall rainfall with RTH over 10 km and lightning frequency increase in the suppressed phase. The rain-yield-per flash (RPF) varies about 20–100% of the mean value of $\sim 2\text{–}10 \times 10^9$ kg fl^{-1} over the tropical warm ocean and that of $\sim 2\text{–}5 \times 10^9$ kg fl^{-1} over the equatorial Islands,

* Corresponding author at: Center for Climate System Research, University of Tokyo, 5-1-5 Kashiwanoha, Kashiwa, Chiba 277-8568, Japan. Tel.: +81 4 7136 4402; fax: +81 4 7136 4375.
E-mail address: yukari@ccsr.u-tokyo.ac.jp (Y.N. Takayabu).
[1] Present address: Japan Weather Association, Tokyo, Japan.

doi:10.1016/j.dynatmoce.2006.02.002

between the convectively suppressed phase and the active phase of MJO, in the manner that RPF is smaller in the suppressed phase and larger in the active phase.

Keywords: Earth atmosphere; Tropical meteorology; Precipitations; Equatorial dynamics; Satellite sensing

1. Introduction

The Madden–Julian oscillation (MJO) is an equatorially trapped eastward propagating disturbance, which has a wave numbers 1–3 and a period of 30–90 days (Madden and Julian, 1971, 1972). It is the most significant atmospheric disturbance associated with cumulus convection in this region. There have been substantial numbers of observational studies about the MJO which are extensively reviewed in Madden and Julian (1994).

Propagating characteristics of the MJO in the eastern hemisphere are different from those in the western hemisphere. In the western hemisphere, the propagation lacks a significant cumulus convection, and its relatively faster propagation ($\sim$20 ms^{-1}) speed is explained basically with dry mode propagation ($\sim$40 ms^{-1}) occasionally obstructed by the topography (e.g., Milliff and Madden, 1996; Matthews, 2000; Kikuchi and Takayabu, 2003). But in the eastern hemisphere, MJO propagates eastward slowly with a speed of about 5 ms^{-1} (e.g., Matthews, 2000). Its propagating characteristics are more complicated because they are tightly coupled with the convective activity and affected by monsoons (e.g. Knutson and Weickmann, 1987; Wang and Rui, 1990). Yanai et al. (2000) showed that MJOs kinetic energy was maintained by a generation of the perturbation available potential energy from the convective heating. But it is not clarified yet why MJO propagates at this speed. To understand the propagation characteristics, it is important to describe the associated convective activity quantitatively.

Most of previous studies of convection with MJO are based on the cloud information such as infrared radiation (IR) and the outgoing longwave radiation (OLR) (e.g., Lau and Chan, 1985, 1986). The internal structure of MJO convective system was studied by Nakazawa (1988). He showed that an eastward propagating MJO with 10,000–20,000 km scale consists of some cloud clusters with several hundred kilometers' scales propagating westward with a period of about 2 days. It was also indicated that these cloud clusters occasionally accompany westward-propagating inertio-gravity wave disturbances of synoptic scales (Takayabu, 1994).

Life cycles of convective activity associated with MJO are intensively investigated utilizing tropical ocean-global atmosphere coupled ocean-atmosphere response experiment (TOGA COARE) network observation data and radar observations. Demott and Rutledge (1998a,b) have examined the vertical structure of rainfall, comparing those in 'inactive' phase and 'organized' phase of the MJO during TOGA COARE intensive operational period (IOP). Interestingly, they showed that although the echo top heights were lower in an 'inactive' phase of the MJO than in 'active' periods, the 'vertically intense' convection is contributing as much. The diabatic heating was also taller in the 'inactive' periods. Lin et al. (2004) also described the evolution of precipitation systems and diabatic heating associated with MJO in TOGA-COARE. They showed that stratiform rain fraction in the total rain increases in the convectively active phase of the MJO.

A gradual development of MJO convective system is also indicated in the moisture field. Kemball-Cook and Weare (2001) showed a water vapor accumulation from the lower layer to the upper layer preceding the active convection using upper-air soundings at stations of the equatorial eastern hemisphere. Kikuchi and Takayabu (2004) showed a stepwise development of MJO cloud top heights and the humidity during TOGA COARE IOP, using infrared T_{BB} histogram data obtained from the Japanese geostationary meteorological satellite and upper-air station data. Recently, Kiladis et al. (2005) analyzed the ERA-15 and station data and described the vertical structure of MJO. They integrated the life cycle of an MJO, as well as other tropical large-scale convective systems, consists of leading shallow convection, central deep organized systems, and trailing stratiform rainfall.

On the other hand, preceding studies indicates that the lightning is produced from the interaction of graupels and ice particles in convective clouds, after cloud tops reach the height about −15 to −20 °C (Takahashi, 1984). Therefore, lightning is a good indicator of very deep convective clouds, and utilized by previous studies to represent characteristics of rain systems. For example, Williams et al. (1992) clarified that the lightning frequency is one order enhanced during the 'break' period of Austral monsoon compared with the 'active' period. They introduced the quantity 'rain yields' or the ratio between the precipitation amount and the lightning frequency and demonstrated its variations between monsoon active-period rain and break-period rain. Zipser (1994) called the ratio as the 'rain thunderstorm ratio (RTR)', and demonstrated that it can be a good index of whether the rain has continental or oceanic features. Petersen and Rutledge (1998) calculated the rain yield for various regions and showed that rain yields varied from $\sim 6 \times 10^7$ kg fl^{-1} for midlatitude arid region, $\sim 4 \times 10^8$ kg fl^{-1} for tropical continental region, to $\sim 1 \times 10^{10}$ kg fl^{-1} for tropical warm Pacific Ocean. More recently, Petersen and Rutledge (2001) utilized TRMM data to study the tropical rain characteristics in terms of lightning and rain top height. Takayabu (2006) calculated a global distribution of the rain-yield per flash (RPF), utilizing TRMM PR and LIS data. In this study, we also utilize simultaneous observation of TRMM LIS and PR to quantitatively obtain the variation of RPF associated with MJO, and locate the MJO rain among various types of the tropical rain.

The purpose of this study is to statistically describe the development of rainfall systems associated with MJO, utilizing the recent availability of the tropical rainfall measuring mission (TRMM) satellite data, as vertical rainrate profiles, convective/stratiform rain amount, latent heating profiles, and lightning. This study is expected to provide important quantitative descriptions of MJO in the eastern hemisphere, for future understandings of their propagation characteristics.

Data used in this study are described in Section 2. Methods are described in Section 3. The rainfall structure and the latent heating associated with MJO are shown in Section 4. Time evolution of MJO convective system is studied in Section 5. Lightning activities associated with MJO precipitation systems are examined in Section 6. Finally, summary and discussion are given in Section 7.

2. Data

The primary dataset used for this study are (1) TRMM precipitation radar (PR) 2A25 Version 5 data, (2) TRMM microwave imager (TMI) 1B11 data, (3) TRMM lightning imaging sensor (LIS) data, (4) latent heating data derived from the spectral latent heating (SLH) algorithm (Shige et al., 2004), and (5) National Oceanic and Atmospheric Administration (NOAA) OLR data.

OLR data, which are conventionally used as a proxy for the cumulus convective activity, are also used to determine the phase of MJO in this study. On the other hand, TRMM PR is the first space-born rain radar to observe the three-dimensional structures of rainfall over ocean and over land. It has about 4.3 km horizontal resolution and 250 m vertical resolution at its nadir point. PR2A25 Version 5 data provide physical properties converted from the radar reflectivity along the orbit. Among them, we utilized three-dimensional distributions of rain rate, near surface rain rate, a rain flag to determine whether the rainfall is convective rain or stratiform rain, and a method flag containing the information for surface conditions. Note that we modify the convective/stratiform rain classifications following the suggestion by Schumacher and Houze (2003); scattered warm rain originally classified to the stratiform rain in the PR2A25 Version 5 data are reclassified to the convective rain.

From TMI 1B11, we use 85.5 GHz data, which has about 6 km horizontal resolution and whose brightness temperature is decreased by scattering with ice particles. In this study, we use polarization corrected temperatures (PCTs) following Spencer et al. (1989) with the parameter beta chosen as 0.45, which gives PCT in the range of 275–290 K. We also utilized the information of lightning occurrences from LIS data. LIS is an optical sensor with a field of view of 550 km × 550 km, with individual pixel resolutions from 3 to 6 km across. Lightning number and view time are provided, so that we can calculate flash rate, by dividing the former by the latter.

Latent heating associated with precipitation is diagnosed from the PR2a25 utilizing the spectral latent heating (SLH) algorithms (Shige et al., 2004). It estimates latent heating profiles from TRMM PR data utilizing a set of tables relating vertical precipitation profiles to latent heating profiles. Those tables are produced from cloud-resolving model (CRM) experiments, forced with large-scale data obtained from field experiments such as tropical ocean and global atmosphere-coupled ocean atmosphere experiments (TOGA-COARE) and global atmospheric research program's Atlantic tropical experiment (GATE).

In order to avoid the influence of the altitude shift of TRMM satellite in August 2001, the analysis period is chosen as from January 1998 to July 2001. The analysis region is basically 0–240°E (120°W), and 20°N–20°S.

3. Analysis method

A life cycle of the eastward-propagating MJO is analyzed with a composite method, referring to the results of extended empirical orthogonal function (EEOF) analysis of OLR during the boreal 'winter' from December to May, prepared by Kikuchi and Takayabu (2005) (personal communication). In their study, the EEOF analysis region was selected as 0–120°W and 40N–30°S. Before calculating the EEOF, 90-day high pass filter and 5-day running mean were applied to the OLR anomaly data from December 1979 to May 2001, and normalized with its standard deviation at each 2.5° × 2.5° grid. Time lags for EEOF were selected as 0, 5 and 10-days, so that the period of extracted systems is expected as about 40-day. After calculating the EEOF, the first two significant EEOFs were projected onto the OLR data for the entire period regardless of winter or summer from 1979 to May 2001, and time series of first two principal components, PC_1 and PC_2 were obtained. Please refer to KT2005 for the propagation patterns of leading two EEOF mode.

In this study, we make a composite life cycle utilizing these PCs obtained in KT2005. First, the phase space of vector $\mathbf{P}(t)$ is calculated as

$$\mathbf{P}(t) = (\mathrm{PC}_1, \mathrm{PC}_2) = |\mathbf{P}(t)|\ \mathrm{e}^{\mathrm{i}\alpha(t)} \tag{1}$$

$$\alpha(T) = \begin{cases} \cos^{-1}\dfrac{\mathrm{PC}_1}{\sqrt{\mathrm{PC}_1^2+\mathrm{PC}_2^2}}, & \mathrm{PC}_2 \geq 0 \\ -\cos^{-1}\dfrac{\mathrm{PC}_1}{\sqrt{\mathrm{PC}_1^2+\mathrm{PC}_2^2}} + 2\pi, & \mathrm{PC}_2 < 0 \end{cases} \tag{2}$$

where t is the time and $\alpha(t)$ is the phase angle of the $\mathbf{P}(t)$, which is from 0 to 2π. Eight phases that divide $\alpha(t)$ equally are defined and all days in the analysis period are assigned to either one of

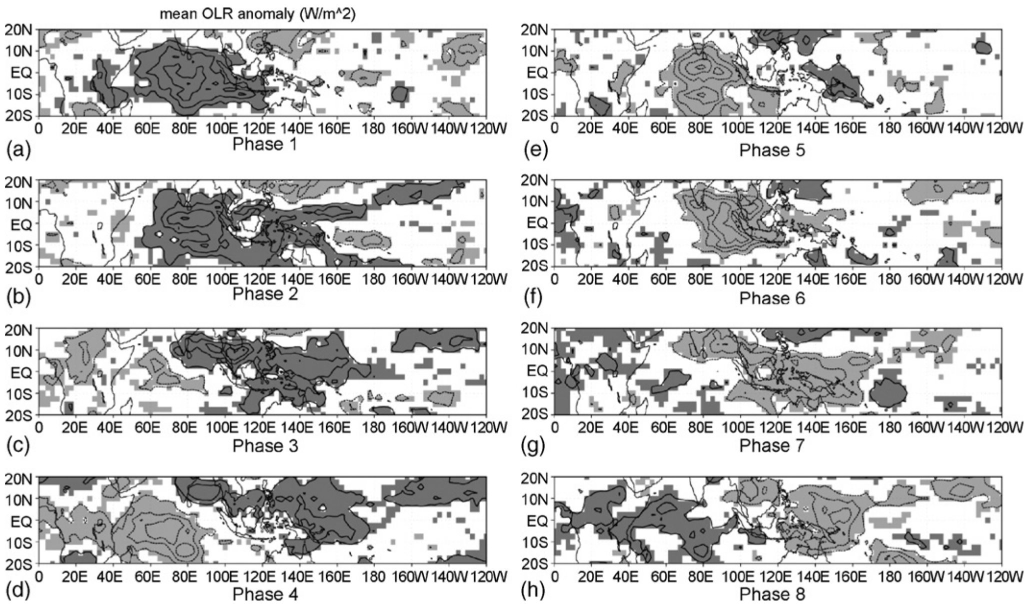

Fig. 1. Composite OLR anomaly distributions for eight phases of MJO determined from the EEOF analysis. Contour intervals are 5 W m^{-2}, and zero contours are suppressed. Dark (light) shades indicate positive (negative) values significant at the 90% confidence levels.

these eight phases. In this study, we do not distinguish significant MJO events from weaker events for the composite, because the analysis period is relatively short (about 3.5 years) and there is a severe limitation in the TRMM PR sampling. In this manner, about 160 days are composited for each phase.

Eight phases of composite OLR anomaly field are shown in Fig. 1, and its longitude-time section for the 10°N–10°S average values are depicted in Fig. 2. There is a clear eastward propagation of

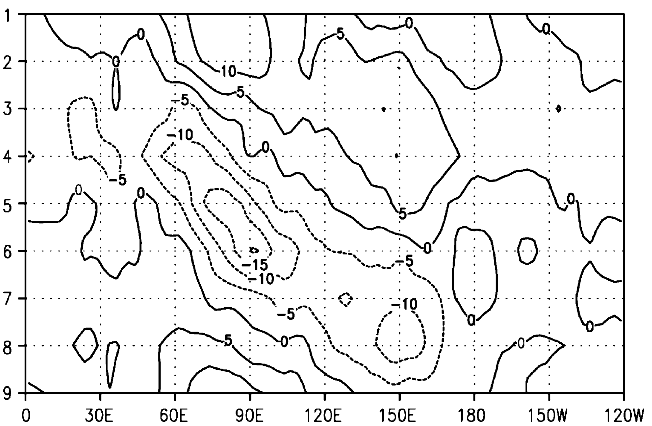

Fig. 2. Longitude-time section of the composite OLR anomaly averaged for 10°N–10°S. The ordinate is the phase which corresponds to the time evolution with one phase interval corresponding to about 5 days. Contour intervals are 10 W m^{-2}, and negative values are depicted with dashed curves.

convective activity from ∼50° to ∼160°E. In phases 1 and 2 (Fig. 1(a) and (b)), Indian Ocean and Maritime Continent are covered with convectively suppressed area. MJO convection represented by OLR minimum, which is indicated by light shades, occurs in phase 3 (Fig. 1(c)) over the western Indian Ocean. It propagates eastward and intensifies during phases 3–5 (Fig. 1(c)–(e)). The center of the convection exists over the eastern Indian Ocean in phase 6 (Fig. 1(f)), and migrates to over the Maritime Continent in phase 7 (Fig. 1(g)). The northward-propagating convection is also seen around India and the Bay of Bengal. At last in phase 8 (Fig. 1(h)), the center of the eastward propagating component is over the equatorial western Pacific. During phases 5–8, the center of the convection propagates at a speed of 5.3 $\mathrm{m\,s^{-1}}$ eastward in average, considering that the phase interval is about 5 days.

Next, we perform two re-composites to show the zonal structure and the time evolution of MJO precipitation systems. Here we assume that the time evolution of MJO precipitation sys-

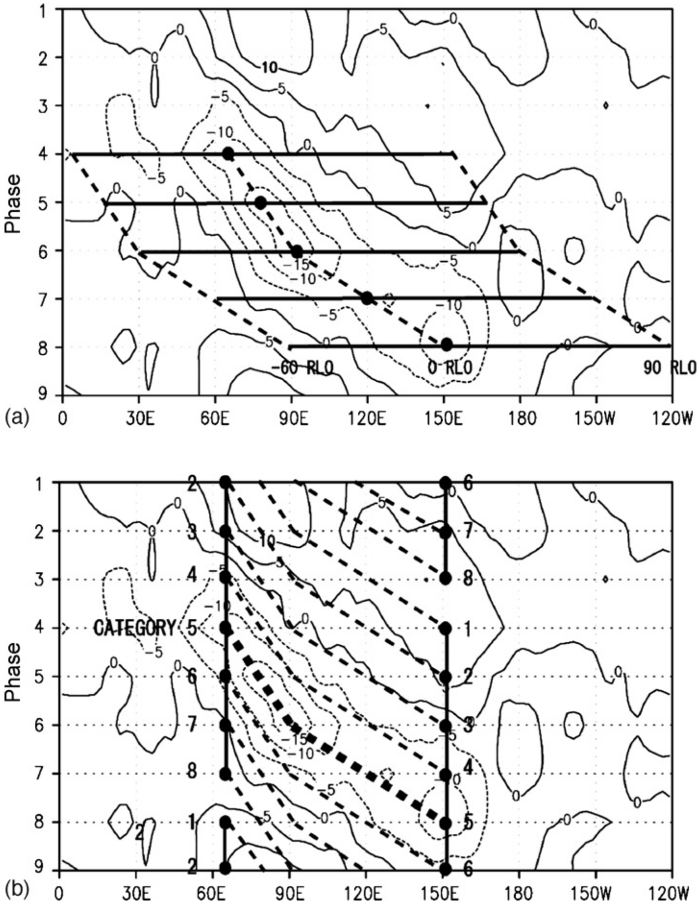

Fig. 3. Schematic illustrations of recomposite method (a) for zonal structure and (b) for the temporal evolution of the MJO. Hovmoller diagram represented by contours is OLR anomaly ($\mathrm{W\,m^{-2}}$) as in Fig. 2. The ordinate is phase and the abscissa is longitude. In (a), a dot indicates the OLR minimum at each phase, and assigned to 0° relative longitude (RLO). A broken line on the left represents −60° RLO and that on the right is for 90° RLO. In (b), the OLR minimum phase at each longitude is assigned to ‘caegory 5’. Other categories are determined relatively with phase. Dashed lines connect the same categories for the composite.

tem is associated with passages of eastward-propagating large-scale convective systems, which themselves do not drastically change their structure in the region between 60–150°E. First, zonal structures of the precipitation systems are obtained by a time-averaging re-composite, with the OLR minimums shifted to the center of composite longitudes as shown in Fig. 3(a). This re-composite is applied for phases between 4 and 8, which are the convectively active phases. The minimum longitudes are 67.5°E at phase 4, 80°E at phase 5, 92.5°E at phase 6, 130°E at phase 7, and 150°E at phase 8. In order to avoid the effects of local conditions such as topography, anomaly fields from the all-phase average at each longitude are used for the composites.

We also perform another zonal-averaging re-composite to obtain the time evolution of the MJO. In order to do so, we first examine at each longitudinal grid of OLR data, whether the minimum of the composite OLR attains the value less than $-5\,\mathrm{W\,m^{-2}}$ somewhere during the eight phases. At the every grid which satisfies that condition, the OLR minimum phase at each longitude is assigned to category 5, and phases before and after this phase are also assigned to categories before and after, in the manner as depicted in Fig. 3(b). Then, physical quantities are re-composited in these categories. The recomposited longitudinal grids are found at 2.5°, 20–37.5° and 50–167.5°E. For some figures, we separately make composites over land and over ocean based on the PR2A25 method flag.

4. Rainfall structure and heating

Longitude-phase sections of stratiform rain ratio anomalies in area (a), and in amount (b), are shown with color shades in Fig. 4. The stratiform rain ratio is larger in the MJO mature phase than in the suppressed phase, where MJO phases are determined with OLR values. The stratiform rain area ratio is ∼5% below average in the mature phase, and ∼5% above average in the suppressed phase, respectively. The amount ratio is ∼8% below and above, on the other hand. These results are consistent with those of Lin et al. (2004) showing the stratiform rain fraction in the MJO is about 0.1 larger than its climatological mean value in the western Pacific and the eastern Indian Ocean.

Fig. 5 shows the re-composite zonal structures of rain rate and OLR anomalies. Both convective rain rate anomaly and stratiform rain rate anomaly increase with MJO, but the amplitude of the stratiform rain rate anomaly is larger by a factor of about 1.7. Overall, anomalous positive precipitation is distributed several degrees to the east of anomalous negative OLR. There are two peaks both in the convective rain and in the stratiform rain, and separations of the peaks are significant for the stratiform rain but marginal for the convective rain. Here, we do not particularly emphasize the existence of two peaks in this analysis. The phase lag between rain and OLR indicates that a massive anvil cloud deck spreads and stays considerably after the substantial precipitation associated with the MJO. A statistically significant secondary precipitation peak is found around 30° to the east of the major OLR peak. Although there is a severe sampling limitation in TRMM PR data, we consider it is not a spurious peak. It is not only because this peak is statistically significant and found both in convective and stratiform rain, but also because there is also found a plateau in the OLR anomaly curve in its vicinity. It is known that an eastward-propagating MJO consists of smaller-scale westward-propagating cloud systems (Nakazawa, 1988). These secondary peaks may suggest that a new internal westward-propagating mesoscale precipitation structure tend to be formed around 30° longitudes ahead of the MJO mature phase.

Next, utilizing the TRMM PR rain rate profiles, vertical distributions of composite convective and stratiform rain rate anomaly are shown in Fig. 6. Here, 1-2-1 smoothing filter in the longitudinal direction is additionally applied, because the rain field is very noisy. Vertically, as consistent with

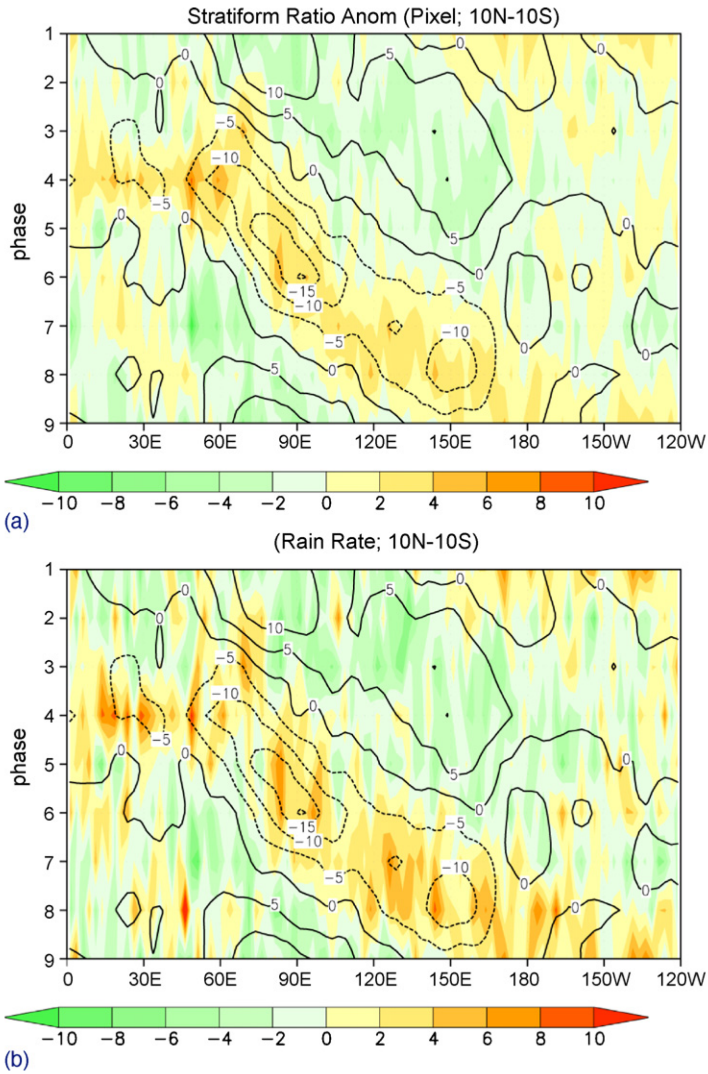

Fig. 4. Longitude-phase sections of (a) the stratiform area ratio and of (b) the stratiform rain amount ratio averaged for 10°N–10°S. Color shades indicate stratiform ratios and contours are for the OLR anomalies as same as in Fig. 1. The unit of color scales are %.

previous radar studies, convective rain rate anomaly has a maximum at around 2–3 km, while stratiform rain rate anomaly has a maximum at around 4.5 km and slightly decreases downward. Horizontally, as seen in the previous Fig. 5, primary convective rain area extends for ∼4000 km zonally from +20° to −15° from the reference. As for the stratiform rain area, while the eastern end is also found ∼+20° similar to the convective rain, the western end extends further westward until −40°. These structures suggest that weak stratiform rain, which evaporates while it falls, spreads as far as about 4000 km behind (or to the west of) the mature stage of the MJO convective system. The secondary peak around ∼+30° mentioned in Fig. 5 is also found in Fig. 6, in both convective and stratiform rain anomalies.

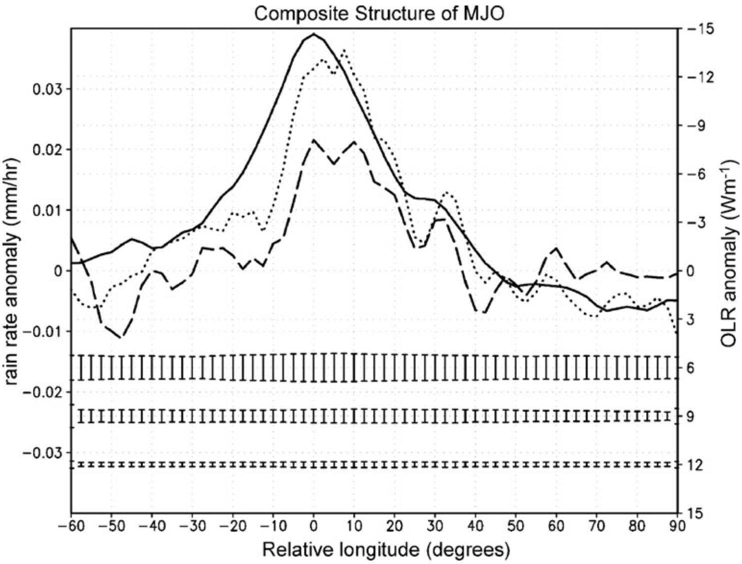

Fig. 5. Longitudinal structure of composite anomalies of OLR (solid line), convective rain rate (broken line) and stratiform rain rate (dotted line), averaged for 10°N–10°S. Labels on the right ordinate are for the OLR anomalies in $\mathrm{W\,m^{-1}}$, and those on the left ordinate are for the rain rate in $\mathrm{mm\,h^{-1}}$. Note that abscissa for the OLR anomaly is flipped. A 5°-longitude running mean filter is applied to the rain data. Error bars (upper bars are for OLR anomaly, middle for convective rain, lower for stratiform rain) show the 95% significance intervals.

In Fig. 7, the vertical structure of composite latent heating anomaly associated with MJO rainfall is illustrated using the SLH-derived latent heating data (Shige et al., 2004). Significant two peak structures at around 3 and 6 km are found in convectively active region from −5° to +15°, and secondarily around +30°. A latent heating maximum exists at ∼10° with a top-heavy heating vertical structure, because there is a considerable contribution from the stratiform rain. From −10° to −32°, there remains weaker but significant positive heating anomaly only in the upper troposphere associated with the remaining stratiform rain. The heating structure which is top-heavy with a trailing heating in the upper troposphere is basically consistent with what obtained by Kiladis et al. (2005). However, the local minimum around freezing level is not found in Kiladis et al. (2005), while the leading gradual increase of heating maximum height is not very clear in our results. Both for the large-scale convective systems (Yoshizaki, 1991a,b) and for the mesoscale convective systems (Mapes and Houze, 1995), it is emphasized that the incorporation of multiple vertical modes associated with vertical heating profiles are substantial for the understanding of the propagation characteristics of the convective systems. In a future study, we should utilize the estimated time series of latent heating for the understanding of MJO propagations.

5. Time evolution of rain systems

In this section, we describe a composite time evolution of MJO rainfall characteristics. Time-series re-composites were made referring to OLR as schematically described in Fig. 3(b). Fig. 8 shows re-composite time series of OLR and 85 GHz PCT anomalies. The interval of categories is about 5 days. OLR anomaly shows a smooth time evolution with the minimum value at category 5, corresponding to the mature phase of MJO convection, and the maximum value at category 1,

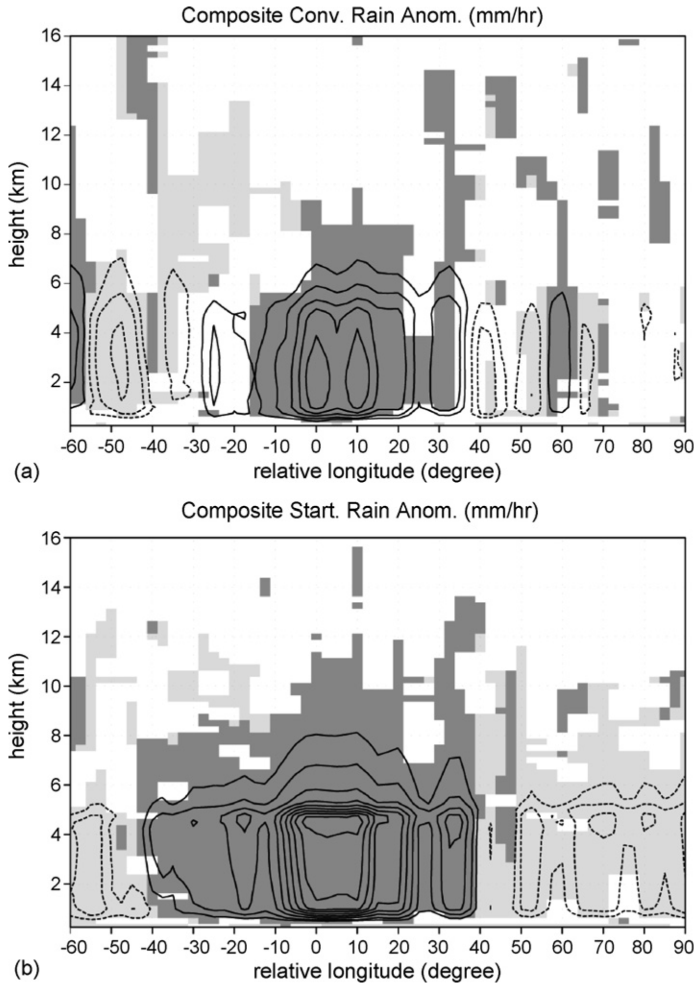

Fig. 6. Longitude-height sections of composite (a) convective rain rate anomaly and (b) stratiform rain rate anomaly averaged from 10°N to 10°S. Contour interval is 0.005 mm h^{-1} except for additional contours for 0.002 mm h^{-1} and -0.002 mm h^{-1}. Zero contours are suppressed. Dark (light) shades indicate positive (negative) values significant at the 95% confidence levels.

corresponding to the suppressed phase. It is shown that the temporal variation of 85 GHz PCT anomaly is almost identical with OLR, indicating that OLR mostly represent the scattering ice particles of the thick and spread anvil clouds.

Next, time series of unconditional mean rain rate for convective rain and stratiform rain are shown in Fig. 9. Fig. 9(a) shows those for total rain rates, which attain their maxima at category 5, and Fig. 9(b) shows rain rate anomaly composites. Although total rain rate of convective rain is 20–30% larger than stratiform rain, the amplitude is larger for the stratiform rain rate. The amplitude of stratiform rain rate anomaly (-0.015 to 0.025) is 1.6 times larger than that of convective rain rate anomaly (-0.009 to 0.014), which is consistent with the result of the previous section (Fig. 7), as well as with Lin et al. (2004).

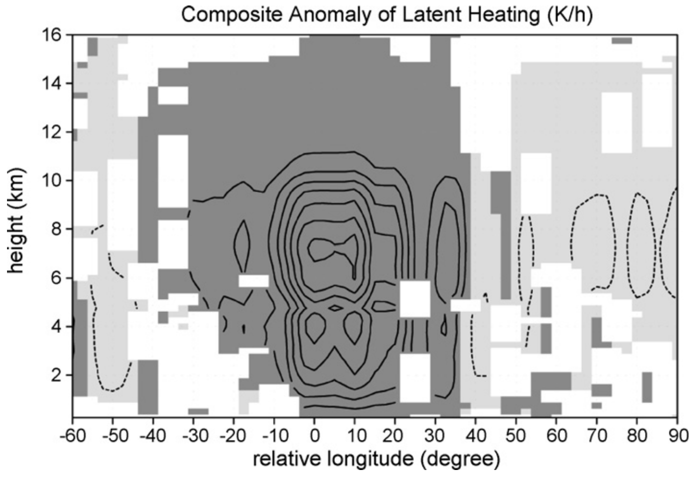

Fig. 7. Same as Fig. 6 but for latent heating anomaly. Contour interval is 0.005 K h^{-1} and zero contours are suppressed.

Fig. 10 compares the re-composite anomalous convective and stratiform rain intensity, over land (solid) and over ocean (dotted). Here, the composite rain intensity corresponds to the conditional mean rain rate under the condition that it is raining. Significant differences are noticed between the time variation of convective rain intensity over ocean and that over land (Fig. 10(a)). Over ocean, the convective rain intensity has a distinct peak at the MJO mature category, category 5. In contrast, it is interesting to find that over land, a largest rainfall intensity of the convective rain is found at category 1 followed by categories 8 and 2, which are in the suppressed phase of MJO referring to the OLR. On the other hand, the stratiform rain intensity is almost constant throughout the MJO lifecycle both over ocean and over land, with its amplitude hardly exceeding

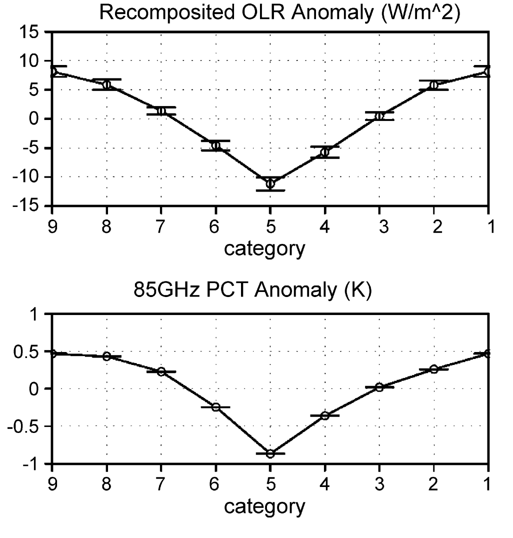

Fig. 8. Composite time series of OLR anomalies and 85 GHz PCT anomalies, averaged from 10°N to 10°S. Time, expressed in categories, is expressed in a manner proceeding from right to left, considering the eastward propagation of MJO. Error bars indicate the 95% significant intervals for the composite values.

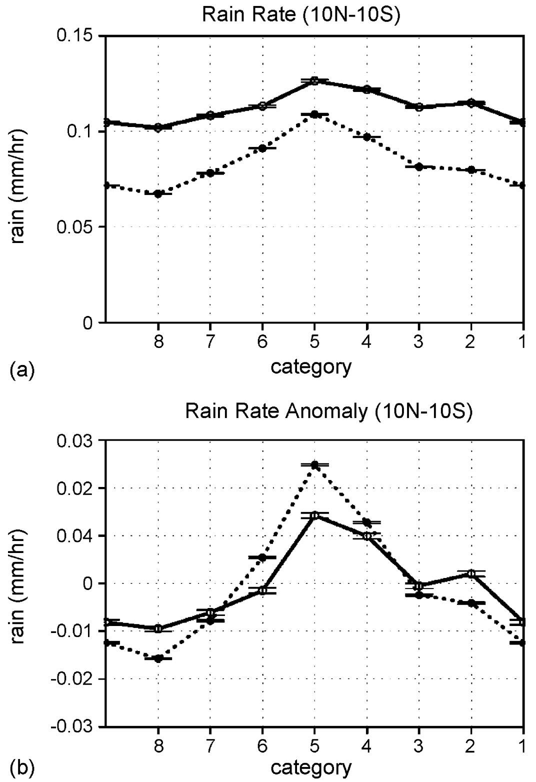

Fig. 9. Same as Fig. 8 but for (a) the rain rate anomaly and (b) the rain rate anomaly. Solid lines represent those for convective rain and dotted lines represent stratiform rain.

$0.1\,\mathrm{mm\,h^{-1}}$ (Fig. 10(b)). It is suggested that stratiform rain, which is mostly maintained with mesoscale dynamics, does not vary very much under different conditions.

With the previous figure, we have shown that convective rain has larger intensity in the MJO suppressed phase over land. Rainfall intensity is closely connected with rain top heights (hereafter referred to as RTH). Therefore, we also compare the RTH anomaly distributions for convective rain and stratiform rain, over ocean and over land in Fig. 11. RTH is determined with a threshold of $0.3\,\mathrm{mm\,h^{-1}}$ rain rate and with a PR2A25 rain-certain flag. Especially conspicuous is quite different RTH variations between over ocean and over land. Over ocean (Fig. 11(a)), two anomaly peaks are found at around 7.5 and 3 km. Higher peak attains its maximum in the MJO mature category 5, while the lower peak does at the suppressed category 1. From categories 3 to 5, there is a slight increase in peak RTH, which is considered to represent the development stage with increasing frequency of deep convection. Then, from categories 5 to 8, there is a gradual decrease of RTH. Over land (Fig. 11(b)), on the other hand, two peaks are found at around 11 and 7 km. Probably, we should consider the latter ~7 km peak over land corresponds to the ~7.5 km peak over ocean, because they both attain maximum values at the MJO mature category 5. These ~7 km RTH peaks are considered to represent the convective rain embedded in well-organized cloud systems, which is accompanied by massive anvil clouds. Anomalous very deep rain with RTH 10–11 km is conspicuous only over land from categories 1 and 2, which is in the MJO suppressed phase. It probably consists of afternoon showers, with very large atmospheric instability over the tropical

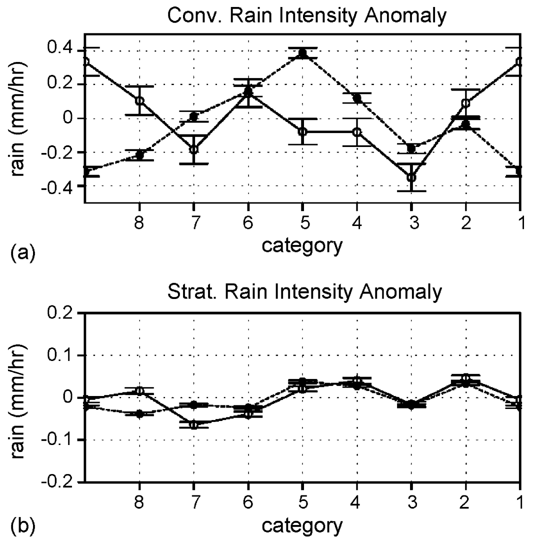

Fig. 10. Composite time series of (a) the convective rain intensity anomaly and (b) the stratiform rain intensity anomaly averaged from 10°N to 10°S. Solid curves are for rain intensity anomalies over land, and dashed curves are for those over ocean. Error bars indicate 95% significance intervals for the composite values. Time, expressed with categories, proceed from right to left as in Fig. 8.

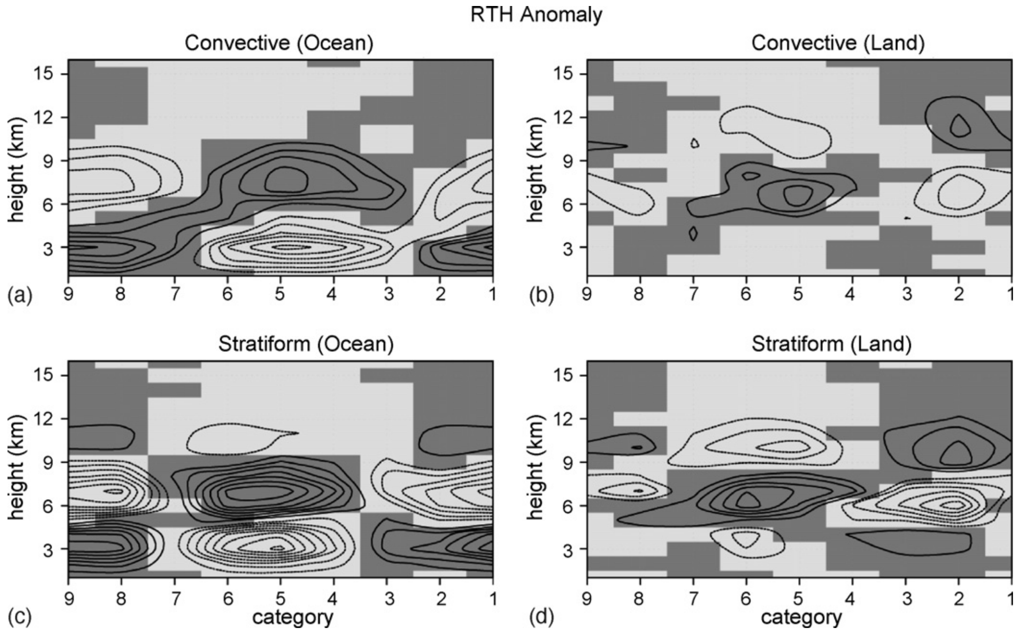

Fig. 11. Time–height sections of the composite rain top height (RTH) anomaly averaged from 10°N to 10°S. Left panels, (a) and (c) are those for over ocean, and those on the right, (b) and (d) are for over land. Also, top panels, (a) and (b) are for the convective rain and bottom, (c) and (d) are for the stratiform rain. Positive (negative) values are depicted with dark (light) shades and solid (dotted) contours. The contour interval is 0.2% and zero contours are suppressed.

continents associated with stronger surface solar heating during the 'suppressed' stage. On the other hand, RTH anomalies over land lack the shallower rain peak at around 3 km, which are ubiquitous over ocean.

As for the stratiform RTHs, in Fig. 11(c) and (d), they show tri-pole structures with peaks at around 10–11, 6–7 and 3–4 km. The positive anomalies of moderately high level (6–7 km) RTH are found from categories 4 to 7, with a maximum at category 6, which lags one category from the convective rain's ~7 km maximum. This 6–7 km RTH anomaly should consist of stratiform rain from the massive anvil shield organized with convective rain with RTH ~7 km. In consistent with the convective rain, the tallest group of rain (RTH > 10 km) is most frequently found in the suppressed phase, phases 8, 1 and 2, and not in the mature phase. Here, the highest RTH anomaly signal is also found over ocean, although weaker, indicating the existence of very tall system even over ocean in the suppressed phase. The shallower stratiform RTH anomaly over land is also found at around 4 km, indicating the top of the shallow system is slightly higher over land than over ocean. This difference in shallow RTH is consistent with the difference in the trade inversion levels over tropical land and tropical ocean described in Takayabu et al. (2006).

To summarize, there are tri-pole RTH levels associated with MJO life cycle, namely, at 10–11, ~7, and ~3 km. These three peaks correspond to the dominance of deep afternoon showers, organized systems, and shallower convection, respectively. During the mature stage of MJO, organized systems with moderate RTH dominates, while during the suppressed stage, sporadic very deep convection and frequent shallow convection are observed. The stratiform rain is basically organized with convective rain, having similar but slightly lower RTH.

6. Lightning activity associated with the MJO precipitation system

In the previous section, it was indicated that rainfall with moderately high RTH (6–9 km) is dominant at the MJO mature phase, and very tall convection with the RTH over 10 km is suppressed. On the other hand, deepest convective rain with RTH over 10 km is found at the MJO suppressed phase, especially over land. For convective rain, RTH at 11 km at category 2 is 10% larger than average, and for stratiform rain, that at 10 km is 15% larger. These results indicate that 'convective activity' expressed with OLR represent well-organized convective systems, but does not really mean the existence of the deepest and the most intense convective rain. In this section, we additionally examine lightning flash rate, which can be considered as another index of the vigor of convection. Lightning flash number and the view time are obtained from the LIS data, and composite flash rate is calculated by dividing the sum of the flash number by the sum of the view time at each location.

Fig. 12 compares the composite time series of the lightning flash rate and the convective rain ratio anomalies. It is notable that large flash rate is found at categories 8, 1 and 2 in the suppressed phase, with a maximum at category 1 with a value of $0.222\,s^{-1}$. The minimum flash rate is found at category 6 in the MJO mature phase with a value of $0.188\,s^{-1}$, which is about 18% lower than the maximum. Lightning events occur more frequently over land than over ocean by the order of 2 (e.g. Nesbitt et al., 2000), so a decrease of lightning events during the mature phase of MJO most probably corresponds with relatively smaller convective rain intensity with a moderate RTH at the mature phase over land as mentioned above. At the MJO suppressed category, on the other hand, the flash rate increases with the rain intensity and RTH over land.

Consistent with the results in the previous section, the convective rain ratio anomaly has a minimum in the mature category 5, and a maximum in the suppressed category 8. The time variation of convective rain ratio and the flash rate is almost parallel, indicating that the intense

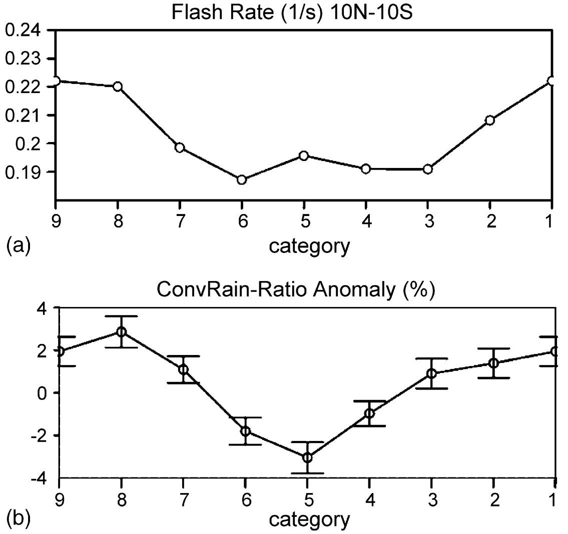

Fig. 12. Same as Fig. 8 but for (a) composite lightning flash rate observed by LIS and (b) composite convective rain ratio anomaly. The unit for the flash rate is s^{-1} and for the rain ratio is %.

deep convection dominates during the suppressed period and the well organized moderate rain dominates during the active period of the MJO. This result is consistent with what described by Demott and Rutledge (1998a,b) that substantial amount of 'vertically intense' convection is observed in the suppressed period.

At last, we compared the value called rain-yield per flash (RPF), which shows amount of rain per one lightning flash. This variable or the same kinds are utilized in previous studies (e.g. Williams et al., 1992; Petersen and Rutledge, 1998; Zipser, 1994; Takayabu, 2006). Petersen and Rutledge (1998, hereafter referred to as PR98) showed that RPF over tropical land is significantly smaller ($\sim 4 \times 10^8$ kg fl^{-1}) than that over tropical warm Pacific Ocean ($\sim 1 \times 10^{10}$ kg fl^{-1}). And also, it is one order smaller in the monsoon break season than in the active season. It means that rain systems in the monsoon mature season have more oceanic characteristics, while those in the break season has more continental characteristics. Fig. 13 compares the OLR anomalies and RPF anomalies at contrasting phases, phases 2 and 6. OLR anomaly composite indicate that, for the region from the eastern Indian Ocean to the Maritime Continent, phase 2 corresponds to the 'suppressed' period in terms of the convective activity, and phase 6 corresponds to the 'active' period, in turn. When we look at the RPF values, on the other hand, it is shown that RPF is larger in the active convective area, and smaller in the suppressed area. The amplitude is about $\pm 2 \times 10^9$ kg fl^{-1} over the eastern Indian Ocean and $\pm 2 \times 10^8$ kg fl^{-1} over the equatorial islands. Fig. 13(c) shows the average RPF distribution for the whole period. The value of $\sim$4–10 $\times 10^9$ kg fl^{-1} is found over the eastern Indian Ocean and over the western Pacific Ocean where large amplitudes at phases 2 and 6 are found. It means that RPF varies about 20–100% of the mean value, between the suppressed phase and the active phase of MJO. In another word, the flash rate for the same amount of rain decreases in the 'active' period, and rain systems tend to show more oceanic characteristics. It is consistent with the previous result that larger flash rate is observed with less rain amount in the suppressed period. It is also similar to what was previously found with the active/break cycle of monsoons (Williams et al., 1992), although it is somehow surprising to find less lightning in the more rainy periods. Note that the RPF values are smaller than those indicated in previous studies.

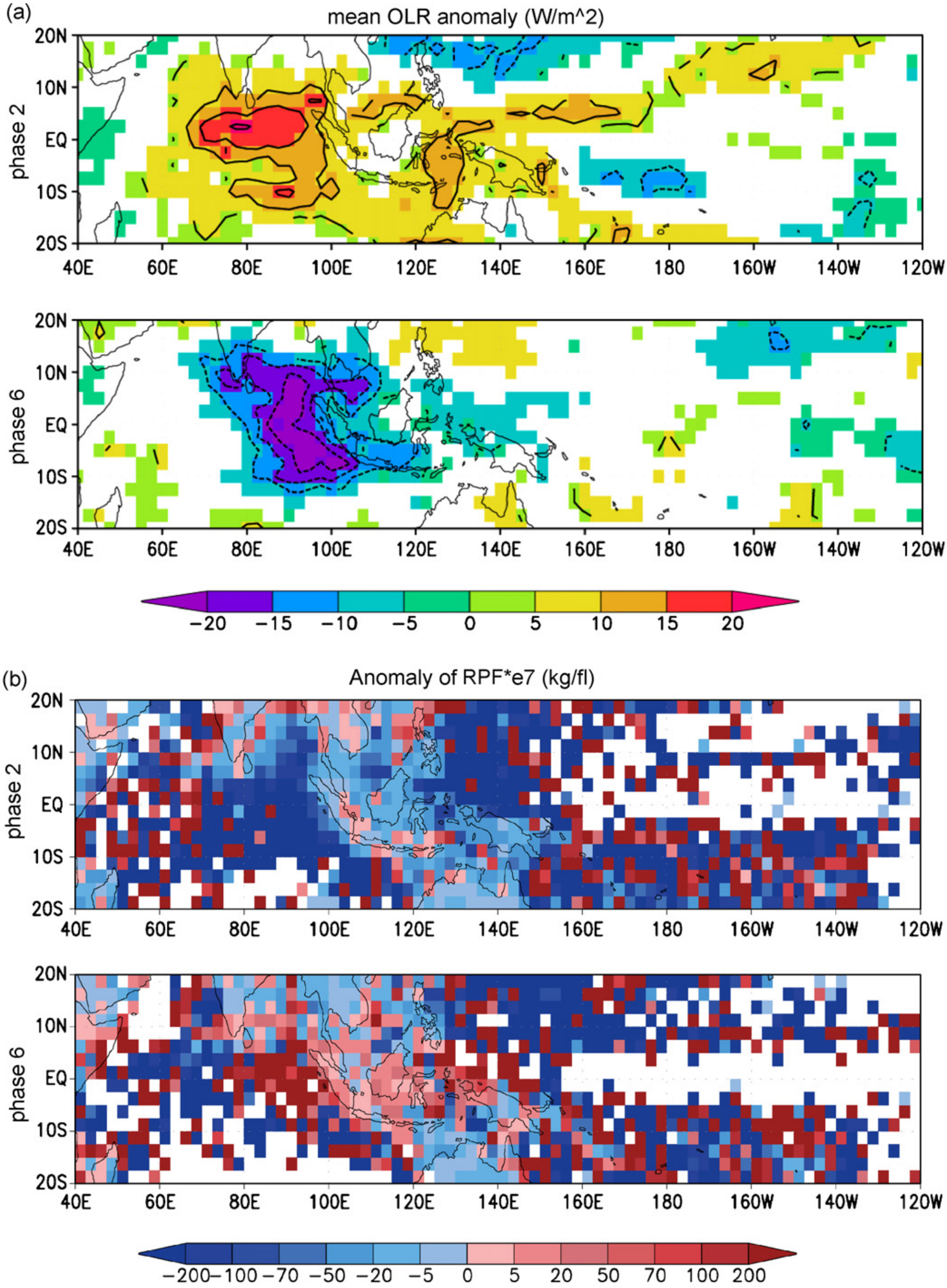

Fig. 13. Comparisons between (a) OLR anomaly distributions and (b) rain-yield per flash (RPF) anomaly distributions for two contrasting phase of MJO, phases 2, and 6. Unit for the color scales are, W m^{-2} for OLR, and 10^7 kg fl^{-1} for RPF. The average RPF distribution for the whole analysis period is also shown in (c), with a unit of 10^7 kg fl^{-1}.

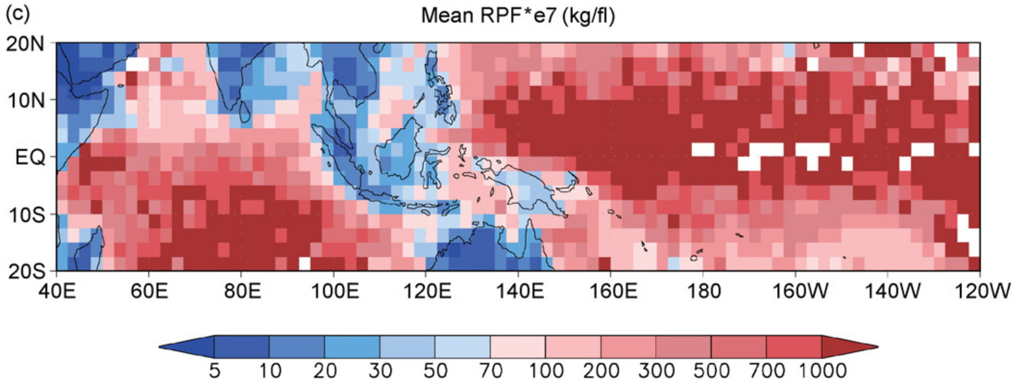

Fig. 13. (*Continued*).

Partially it is because only the cloud-to-ground lightning flash number is utilized in PR98, besides the difference in instruments. It is also interesting to note that RPF varies substantially with MJO not only over land but also over the ocean, as shown over the eastern Indian Ocean in Fig. 13(b).

After all, it is shown that rain systems with lightning tendency show more oceanic characteristics in the mature phase of the MJO, while they have more continental characteristics in the suppressed phase. It is in a similar sense with those variations with monsoon active/break cycles, but it is notable that such variation of rain–lightning characteristics is observed significantly not only over the land but also over the ocean in association with the MJO.

7. Summary and discussions

In this study, we have analyzed the rainfall characteristics associated with the MJO using the TRMM data. As a result, the analysed variation of rainfall systems with the MJO is schematically summarized in Fig. 14. The life cycle of MJO is illustrated to consist of four stages; suppressed, developing, mature, and decaying stages. And three typical rain-top heights (RTH) are shown at ∼3 and ∼7 and 10–11 km. Note that the schematic clouds are depicted slightly taller than typical RTH. High cloud cover shown by OLR, convective rain, and stratiform rain all shows maximum values in the mature phase, while both the developing stage and the decaying stage are observed earlier for rain than the cloud cover. The amplitude of stratiform rain is ∼1.7 times larger than convective rain, and the stratiform rain remains longer than the convective rain in the decaying stage. These features result in the development of top-heavy latent heating distribution toward mature and decaying stages.

In the MJO mature stage, large-scale (over 1000 km) field is mostly cloudy as indicated with low OLR. In this stage, well-organized mesoscale convective systems with moderately high (∼7 km) RTH dominate, associated with less lightning. In the MJO suppressed stage, on the other hand, large-scale field is less cloudy. At this phase, especially over land, not well organized but very tall (over 10 km) afternoon showers with frequent lightning dominate. The dominance of lightning in the suppressed period of MJO is in concert with a finding by Williams et al. (1992) that lightning activity is higher during the ‘break’ period than the ‘active’ period of the Australian monsoon. Why a large amount of rain with moderately high RTH is preferred in the MJO mature stage, instead of deepest rain with RTH over 10 km, is an interesting problem for future work related to the role of cloud clusters embedded in the MJO (Nakazawa, 1988; Takayabu, 1994).

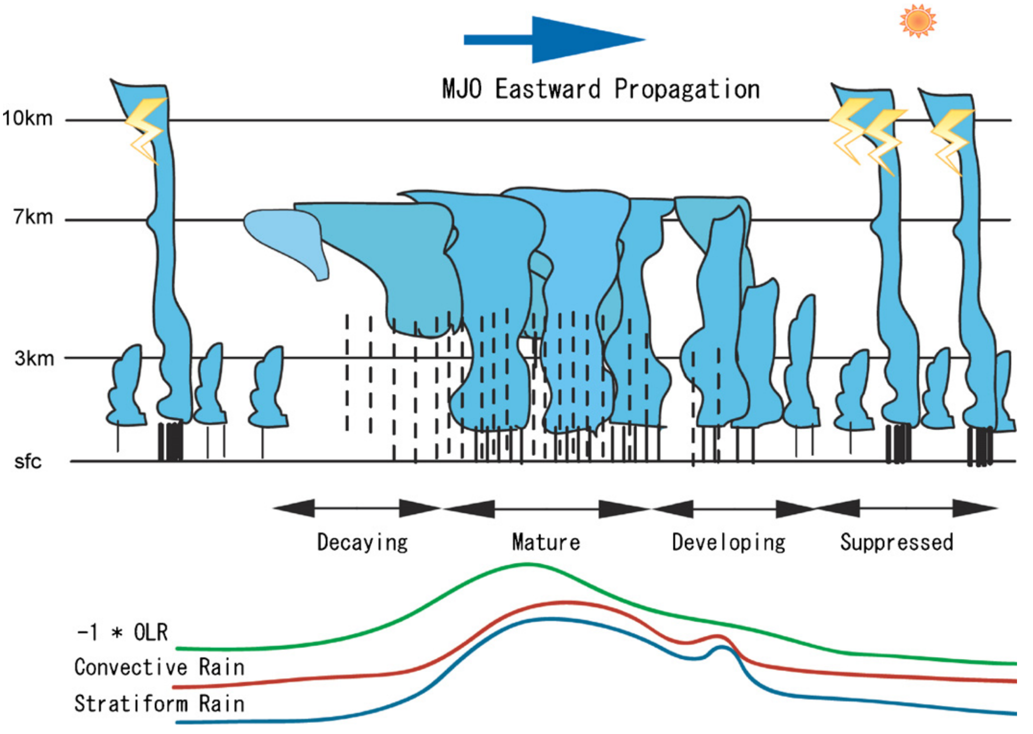

Fig. 14. Conceptual model of an MJO life cycle in terms of rain and rain-related variables. Vertical solid lines represent convective rainfall and vertical dashed lines represent stratiform rainfall. Since it is assumed that the system moves eastward without drastically changing the structure in this analysis area, the abscissa represents longitudes as well as time. And time proceeds from right to left. The three curves in the bottom schematically represent anomalies of the inverse of OLR, the convective rain amount, and the stratiform rain amount, from top to bottom.

This study also has exhibited the evolution of latent heating distribution with the MJO using the SLH-derived latent heating data (Shige et al., 2004) from TRMM PR observation. It is an important information in considering the propagation of the MJO from a dynamical viewpoint. To examine the propagation characteristics of the MJO using the observed latent heating distribution is also left for future studies.

A schematic model of the rainfall characteristics of the MJO is given. However, since we utilized composite analyses to overcome the insufficient sampling of TRMM PR, the life cycle of individual mesoscale rainfall system which is embedded in the MJO could not be precisely studied. Future global precipitation measurement (GPM) with finer temporal samplings may enable us to study life cycles of mesoscale rainfall systems associated with the MJO. With such studies, further understandings of the role of mesoscale convective systems embedded in the MJO will be expected.

Acknowledgements

The first author expresses special thanks to Dr. Kazuyoshi Kikuchi for his providing EEOF data and useful advices. The authors thank Prof. Tomoo Ushio to provide TRMM LIS data, and Dr. Kazumasa Aonashi to provide TRMM TMI data. Constructive comments by anonymous reviewers and the editor Dr. George Kiladis were gratefully appreciated. This study is supported by the Grants-in-Aid for Scientific Research on Priority Area – 764 of the Ministry of Education, Culture, Sports, Science and Technology (MEXT) of Japan, and TRMM JRA4 by the Japan Aerospace Exploration Agency.

References

Demott, C.A., Rutledge, S.A., 1998a. The vertical structure of TOGA COARE convection. Part I. Radar echo distributions. J. Atmos. Soc. 55, 2730–2747.

Demott, C.A., Rutledge, S.A., 1998b. The vertical structure of TOGA COARE convection. Part II. Modulating influences and implications for diabatic heating. J. Atmos. Soc. 55, 2748–2762.

Kemball-Cook, S.R., Weare, B.C., 2001. The onset of convection in the Madden–Julian oscillation. J. Climate 14, 780–793.

Kikuchi, K., Takayabu, Y.N., 2003. Equatorial circumnavigation of moisture signal associated with the Madden–Julian oscillation (MJO) during boreal winter. J. Meteor. Soc. Jpn. 81, 851–869.

Kikuchi, K., Takayabu, Y.N., 2004. The development of organized convection associated with the MJO during TOGA COARE IOP: trimodal characteristics. Geophys. Res. Lett. 31, L10101, doi:10.1029/2004GL019601.

Kiladis, G.N., Straub, K.H., Haertel, P.T., 2005. Zonal and vertical structure of the Madden–Julian oscillation. J. Atmos. Sci. 62, 2790–2809.

Knutson, T.R., Weickmann, K.M., 1987. 30–60 day atmospheric oscillations: composite life cycles of convection and circulation anomalies. Mon. Weather Rev. 115, 1407–1436.

Lau, K.M., Chan, P.H., 1985. Aspects of the 40–50 day oscillation during the northern winter as inferred from outgoing longwave radiation. Mon. Weather Rev. 113, 1889–1909.

Lau, K.M., Chan, P.H., 1986. Aspects of the 40–50 day oscillation during the northern summer as inferred from outgoing longwave radiation. Mon. Weather Rev. 114, 1354–1367.

Lin, J., Mapes, B., Zhang, M., Newman, M., 2004. Stratiform precipitation, vertical heating profiles, and the Madden–Julian oscillation. J. Atmos. Sci. 61, 296–309.

Madden, R.A., Julian, P.R., 1971. Detection of a 40–50 day oscillation in the zonal wind in the tropical Pacific. J. Atmos. Sci. 28, 702–708.

Madden, R.A., Julian, P.R., 1972. Description of global-scale circulation cells in the tropics with a 40–50 day period. J. Atmos. Sci. 29, 1109–1123.

Madden, R.A., Julian, P.R., 1994. Observations of the 40–50-day tropical oscillation—a review. Mon. Weather Rev. 122, 814–837.

Mapes, B.E., Houze Jr., R.A., 1995. Diabatic divergence profiles in western Pacific mesoscale convective systems. J. Atmos. Sci. 52, 1807–1828.

Matthews, A.J., 2000. Propagation mechanisms for the Madden–Julian oscillation. Q. J. Roy. Meteor. Soc. 126, 2637–2651.

Milliff, R.F., Madden, R.A., 1996. The existence and vertical structure of fast, eastward-moving disturbances in the equatorial troposphere. J. Atmos. Sci. 53, 586–597.

Nakazawa, T., 1988. Tropical super clusters within intraseasonal variations over the western Pacific. J. Meteor. Soc. Jpn. 66, 823–839.

Nesbitt, S.W., Zipser, E.J., Cecil, D.J., 2000. A census of precipitation features in the Tropics using TRMM: radar, ice scattering, and lightning observations. J. Climate 13, 4087–4106.

Petersen, W.A., Rutledge, S.A., 1998. On the relationship between cloud-to-ground lightning and convective rainfall. J. Geophys. Res. 103 (D12), 14025–14040.

Petersen, W.A., Rutledge, S.A., 2001. Regional variability in tropical convection: observations from TRMM. J. Climate 14, 3566–3586.

Schumacher, C., Houze Jr., R.A., 2003. The TRMM precipitation radar's view of shallow, isolated rain. J. Appl. Meteor. 42, 1519–1524.

Shige, S., Takayabu, Y.N., Tao, W.-K., Johnson, D.E., 2004. Spectral retrieval of latent heating profiles from TRMM PR data. Part I. Development of a model-based algorithm. J. Appl. Meteor. 43, 1095–1113.

Spencer, R.W., Goodman, H.M., Hood, R.E., 1989. Precipitation retrieval over land and ocean with the SSM/I: identification and characteristics of the scattering signal. J. Atmos. Oceanic Technol. 6, 254–273.

Takahashi, T., 1984. Thunderstorm electrification—a numerical study. J. Atmos. Sci. 41, 2541–2557.

Takayabu, Y.N., 1994. Large-scale cloud disturbances associated with equatorial waves. Part II. Westward-propagating inertio-gravity waves. J. Meteor. Soc. Jpn. 72, 451–465.

Takayabu, Y.N., 2006. Rain-yield per flash calculated from TRMM PR and LIS data and its relationship to the Tall Convective Rain Contributions. Geoph. Res. Lett., in press.

Takayabu, Y.N., Yokomori, J., Yoneyama, K., 2006. A diagnostic study on interactions between atmospheric thermodynamic structure and cumulus convection over the tropical western Pacific Ocean and over the Indochina Peninsula. J. Meteor. Soc. Japan 84A, 151–169.

Wang, B., Rui, H., 1990. Synoptic climatology of transient tropical intraseasonal convection anomalies: 1975–1985. Meteor. Atmos. Phys. 44, 43–61.

Williams, E.R., Rutledge, S.A., Geotis, S.G., Renno, N., Rasmussen, E., Rickenback, T., 1992. A radar and electrical study of tropical 'hot towers'. J. Atmos. Sci. 49, 1386–1395.

Yanai, M., Chen, B., Tung, W.-w., 2000. The Madden-Julian oscillation observed during the TOGA COARE IOP: global view. J. Atmos. Sci. 57, 2374–2396.

Yoshizaki, M., 1991a. Selective amplification of the eastward-propagating mode in a positive-only wave-CISK model on an equatorial beta plane. J. Meteor. Soc. Jpn. 69, 353–373.

Yoshizaki, M., 1991b. On the selection of eastward-propagating modes appearing in the wave-CISK model as tropical intraseasonal (30–60 day) oscillations—linear responses to localized heating moving in the east–west direction on the equatorial beta plane. J. Meteor. Soc. Jpn. 69, 595–608.

Zipser, E.J., 1994. Deep cumulonimbus cloud systems in the tropics with and without lightning. Mon. Weather Rev. 122, 1837–1851.